Mechanistic analysis of coal permeability evolution data under stress-controlled conditions

Rui Shi[a,b], Jishan Liu[c,*], Mingyao Wei[d], Derek Elsworth[e], Xiaoming Wang[a]

[a] Key Laboratory of Tectonics and Petroleum Resources, Ministry of Education, China University of Geosciences, Wuhan 430074, China
[b] Beijing Key Laboratory for Precise Mining of Intergrown Energy and Resources, China University of Mining and Technology, Beijing 100083, China
[c] Department of Chemical Engineering, School of Engineering, The University of Western Australia, 35 Stirling Highway, WA 6009, Australia
[d] State Key Laboratory of Geomechanics and Geotechnical Engineering, Institute of Rock and Soil Mechanics, Chinese Academy of Sciences, Wuhan 430071, China
[e] Department of Energy and Mineral Engineering, G3 Centre and Energy Institute, The Pennsylvania State University, University park, PA 16802, USA

ARTICLE INFO

ABSTRACT

At present, two types of experiments under stress-controlled conditions were normally conducted to measure coal permeability: constant confining pressure (CCP) tests and constant effective stress (CES) ones. The original rationale of this situation was to assume that the impacts of effective stresses and gas sorption-induced matrix swelling/shrinking on coal permeability could be separated and investigated individually. In this study, we collected coal permeability data measured under both conditions with a purpose to see if this original rationale was appropriate. This goal was achieved through collection of experimental permeability data under the CCP conditions; collection of experimental permeability data under the CES conditions; and comparison of those experimental data with solutions of the poroelastic theory. For CCP tests, the permeability ratios change from reductions (less than 1.0) to enhancements (greater than 1). These changes are bounded by an upper envelope and a lower one. The upper envelope is corresponding to the solution of free-swelling while the lower one zero-swelling. For CES tests, the permeability ratios also change within an upper envelope and a lower one. The upper envelope is equal to 1.0 corresponding to the solution of free-swelling while the lower one zero-swelling. Through these comparisons, we found that permeability data for both types of tests are confined within the poroelastic solutions for two extreme boundary conditions: free-swelling and zero-swelling. These findings suggest that permeability ratios for both constant confining tests and constant effective stress tests are primarily determined by the matrix-fracture interactions, including sorption-induced swelling/shrinking, through transient effective stresses in matrixes and fractures.

1. Introduction

Coal permeability experiments can be divided into displacement controlled ones and stress controlled ones. For displacement-controlled experiments, uniaxial strain experiments are normally used to study the evolution of coal permeability. Many permeability models under uniaxial strain conditions were derived,[1–6] and the most widely used is proposed by Palmer and Mansoori,[3] some scholars have further proved it [7,8]. Although these permeability models are under uniaxial strain conditions but only a few of experiments are under these conditions.[9–11]

As for the stress controlled condition experiments, two types of experiments are normally conducted to investigate the impact of coal deformation on the evolution of coal permeability. One is to keep the total stress as constant while the other is to keep the effective stress as constant. When the total stress is constant, the effective stress decreases

as the gas pressure increases. Under this condition, the effective stress is believed to be the important reason for the evolution of coal permeability. When the effective stress is constant (this can be achieved through keeping the increment of total stress the same as that of gas pressure), the effective stress impact is eliminated. Under this condition, the gas sorption is believed to be the important reason for the evolution of coal permeability. These two hypotheses have been guiding the experimental research of coal permeability for decades.

The primary goal of CCP tests is to measure the influence of effective stress and associated processes on the evolution of coal permeability. For examples, CCP tests were used to investigate the impact of effective stress and the combined adsorption/desorption effect on the evolution of permeability;[10,12–22] to simulate the change of permeability in CO_2-ECBM process;[23,24] to investigate the temperature effect on permeability;[25,26] to study the influence of fracture geometry and water-

content on permeability;[27,28] to study the influence of cleat volume compressibility on permeability;[16] to study the influence of slippage effect[29] on permeability;[16–18] to study the permeability evolution of propped artificial fractures in coal on injection of CO_2,[30] and study the dynamic permeability in the process of gas injection/depletion.[31–33] These examples illustrate the importance of CCP tests in a broad spectrum of applications. In all of these studies of gas injection condition, coal permeability data can be classified as three categories: permeability increases directly with the increasing of injection pressure;[12–15,23,25,27,30] permeability decreases initially with the increasing of injection pressure, and then rebounds;[14,27,30] and permeability decreases with the increasing of injection pressure and nearly show no rebound.[16,17] In all of these studies of gas depletion condition, coal permeability data can also be classified as three categories: permeability decreases directly with the decreasing of pore pressure;[10,13,34] permeability decreases initially with the decreasing of pore pressure, and then rebounds lower than the initial permeability;[10,12] permeability decreases initially with the decreasing of pore pressure, and then rebounds larger than the initial permeability.[12,13,18,35]

The primary goal of CES tests is to measure the influence of gas adsorption/desorption on the evolution of coal permeability and the associated processes. For examples, the CES tests were conducted to investigate the impact of gas adsorption/desorption on the evolution of permeability.[2,36–47] Some previous studies use CES tests to study the influence of the size of effect stress on permeability.[2,38,40] The CES tests were also used to investigate the effect of slippage effect on permeability,[36,38–40] and the sensitivity of permeability to pore pressure.[48] Different from the CCP tests all of the permeability data from the CES tests decrease with the increasing of pore pressure, but the declining rate is different.

A number of permeability models were developed to explain the experimental observations and have been reviewed.[1,3,5,8,15,49–53] In our previous work,[54] we concluded that these models can't explain the results from stress-controlled laboratory tests (CCP tests and CES tests). Both the hypotheses and permeability models are based on the theory of single poroelasticity but applied to explain the experimental data for a typical dual porosity and dual permeability system. These experiments were conducted under the triaxial conditions, while most permeability models were developed under specific conditions such as uniaxial strains. The experimental observations cannot be explained unless these inconsistencies are resolved.

When a dual porosity system such as coal is assumed as the single poroelastic medium, we hypothesize that the gas pressures between the fracture and matrix has reached equilibrium. This is why we have to measure the coal permeability at the equilibrium state when we use the theory of single poroelasticity. This could take from a few days[36] to a few weeks.[16] When the gas sorption was included, the time from the initial state to the final equilibrium state might take much longer from a few months to years.[23,34]. When coal is assumed as a dual porosity system, we hypothesize that the gas pressures between the fracture and matrix reach equilibrium gradually. We assume that the matrix pressure changes as a function of time. We do not consider the pressure gradient in the matrix for permeability models. These assumptions were implemented in the theoretical analysis of permeability evolution but we still measure the permeability at the equilibrium state.[55] Because we measure the permeability only at the equilibrium state, the impact of interactions between matrix and fracture has been excluded and the permeability data can be explained by using the theory of single poroelasticity.

In this study, we hypothesize that if the experimental observations are the permeability at the equilibrium state, the permeability data should be consistent with the theory of single poroelasticity. We test this hypothesis through collecting all of permeability data at the equilibrium state available in the literature, comparing them with the theoretical solutions of single poroelasticity, and conducting a mechanistic analysis of these comparisons. These results and findings are reported in the following sections.
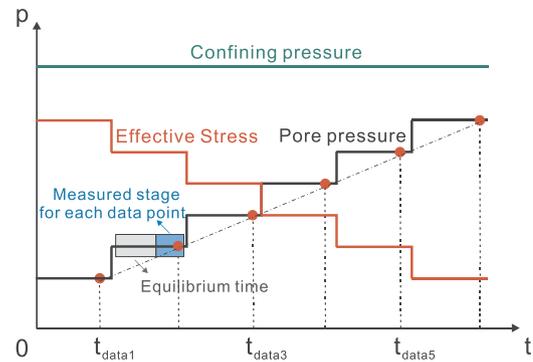
Fig. 1. Schematic diagram of the experimental process during gas injection for CCP tests.

2. Experimental permeability under constant confining pressure

2.1. Data collection

In this section, we collected the experimental permeability data under the condition of constant confining pressure. In these experiments, the confining pressure was maintained as constant (green line) while the gas pressure (black line) increased/decreased from a lower/larger value to a larger/lower one, then the effective stress (red line) decreased/increased gradually with the increasing/decreasing of pore pressure, as shown in Fig. 1 for gas injection condition. The gray rectangular in the pore pressure line is the time needed to reach the equilibrium state, and the blue rectangular in the pore pressure line is the measured stage for each data point (red point) at time t_{data-x}. Gas permeability was calculated using the modified Darcy's law for a compressible gas.[56] Permeability was measured either by the steady-state method or the pressure transient one. For the purpose to study the impact of coal deformation on the evolution of coal permeability, the data by using other methods[57] are not included.

Steady State Method: The specific implementation mode of steady state method is shown in Fig. 2(a). The black vertical axis is the pressure value, and the blue vertical axis is the flow rate which only indicates the blue flow rate line. In a typical steady state experiment, the sample is placed into the triaxial core holder and both confining pressure and axial stresses are applied at a slow rate to establish initial conditions and are then kept constant (green line). The sample is then vacuum desaturated to evacuate air from the system. The sample is then flushed with the fluid to be used to an equilibrium state (light gray line), as an initial condition that it is considered that the pressure distribution in sample is evenly balanced (light gray rectangular, $p_{up} = p_{dn}$). A pressure increment (Δp) is then applied to the upstream gas reservoir (light red line and red line) and keeps constant for each data measurement. The downstream pressure (gray line) is consistent with the initial condition. The flow rate of the upstream or the downstream is measured. The flow rate first increases slowly (light blue line) and then keep constant (blue line). The measured stage is started at time t_{test}, and when the flow rate is stable for enough time the pressure and flow rate data are available at time t_{data} (red points). And it is considered that the pressure distribution in sample is declining linearly from the upstream to the downstream (gray gradient rectangular, $p_{up} > p_{dn}$).

Permeability of the coal sample to gas was calculated according to the compressible form of Darcy's law,

$$k = \frac{2Q_a P_a \mu L}{A(P_{up}^2 - P_{dn}^2)} \tag{1}$$

where k is the permeability (mD), Q_a is the volumetric rate of flow at reference pressure P_a (cm^3/s), P_a is the reference pressure (Pa), μ is the fluid viscosity (cp), L is the core sample length (cm), A is the cross-
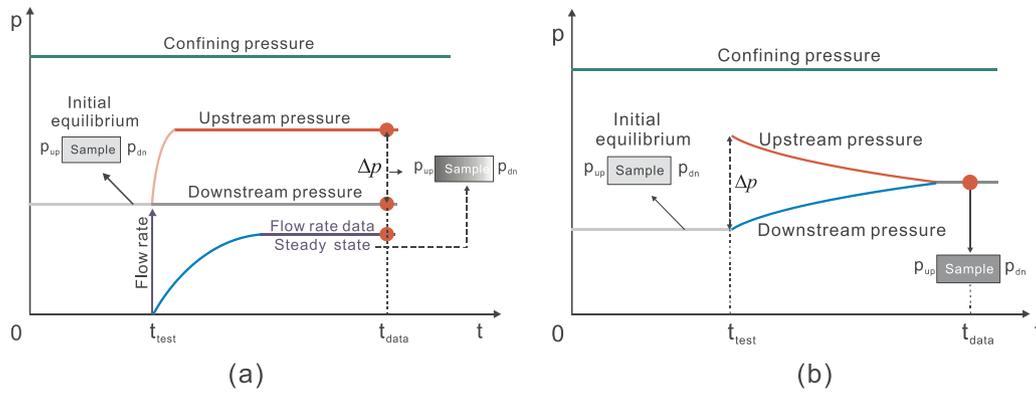
Fig. 2. Schematic diagram of the steady state experimental method and pressure transient experimental method.
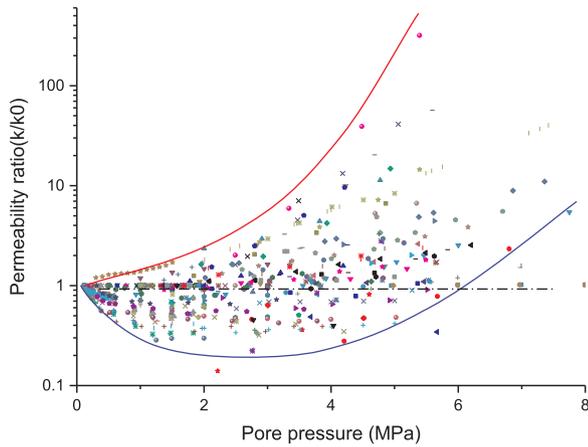
Fig. 3. Statistical distribution of coal permeability ratios during gas injection for CCP tests.

section area of the core sample (cm²), P_{up} is the upstream pressure (Pa), and P_{dn} is the downstream pressure (Pa).

Pressure Transient Method: The specific implementation mode of pressure transient method is shown in Fig. 2(b). In a typical pressure transient experiment, the sample is placed into the triaxial core holder and both confining pressure and axial stresses are applied at a slow rate to establish initial conditions and are then kept constant (green line). The sample-reservoir system is then vacuum desaturated to evacuate air from the system. The sample is then flushed with the fluid to be used and, as an initial condition, reservoirs and sample are equilibrated with a fluid at the same pressure (light gray line). It is considered that the pressure distribution in sample is evenly balanced at this state (light gray rectangular, $p_{up} = p_{dn}$). A pressure increment (Δp) is then applied to the upstream gas reservoir and discharged through the sample to the downstream gas reservoir. The time taken for the discharging upstream reservoir (red line) and the recharging downstream reservoir (blue line) to reach a new equilibrium pressure (gray line) is measured. It is considered that at this state the pressure distribution in sample is evenly balanced too (gray rectangular, $p_{up} = p_{dn}$). The pressure decay rate recorded in the upstream reservoir and the pressure increase rate in the downstream reservoir are used to evaluate permeability. The decay characteristics depend on the permeability, on the dimensions of the sample and reservoirs, and on the physical characteristics of the permeating fluid.[15,27]

The transient method of Brace was widely used to conduct the gas flow experiments in the low permeability samples. The Brace method involves observing the decay of a differential pressure between upstream and downstream vessels across the sample. This pressure decay is combined with the vessel volumes in the analysis to relate the flow through the sample and thus determine the permeability.[58] The

pressure decay curve can be modeled as:

$$\frac{p_{up}(t) - p_{dn}(t)}{p_{up}(t_0) - p_{dn}(t_0)} = e^{-\upsilon t}$$

(2)

$$\upsilon = \frac{kA}{\mu \beta L}(1/V_{up} + 1/V_{dn})$$

(3)

where $P_{up}(t) - P_{dn}(t)$ is the pressure difference between the upstream and downstream reservoirs at time t, (Pa); and $(P_{up}(t_0) - P_{dn}(t_0))$ is the initial pressure difference between the upstream and downstream reservoirs at time t_0, (Pa). υ is the slope of the line when plotting the pressure decay $P_{up}(t) - P_{dn}(t)$ on semi-log paper against time. L is the core sample length (cm), A is the cross-section area of the core sample (cm²), μ is the fluid viscosity (cp), β is the compressibility of the gas, and V_{up} and V_{dn} are the volume of the upstream reservoir and downstream reservoir respectively, (cm³).

For the case of gas injection, we use the lowest gas pressure in an experiment as the initial pore pressure. The permeability ratio is defined as the ratio of permeability at the initial pressure to that at the current one. All experimental permeability ratios under constant confining pressures are shown in Fig. 3 where the details of the data sources are shown in Table 1. Although they spread over a wide range of magnitudes, they are within a lower bound and an upper one. These experimental data represent a wide range of permeability measurements with different gases such as helium, argon, nitrogen, methane and carbon dioxide. The injection pressure varies from 0.1 to 8.0 MPa while the confining pressure from 3.0 to 40.0 MPa.

For the case of gas depletion, we use the highest gas pressure in an experiment as the initial gas pressure. The permeability ratio is defined as the ratio of permeability at the initial pressure to that at the current one. As shown in Fig. 4, although all experimental permeability ratios spread over a wide range of magnitudes, they are within a lower bound and an upper one. The details of the data sources are shown in Table 2. These experimental data represent a wide range of permeability measurements with different gases such as helium, methane and carbon dioxide. Most data points are within the zone of permeability ratio less than 1.0. The pore pressure varies from 0.2 to 6.8 MPa while the confining pressure from 3.0 to 13.8 MPa.

2.2. Impact of confining pressure magnitude

According to the magnitude of confining pressure, the distribution of permeability ratios can be divided into three zones from lower confining pressure to higher ones for the case of gas injection. When the gas pressure (from 0 to 2 MPa) is lower, nearly all high confining pressure (> 5 MPa) data points are below the $k/k_0 = 1$ line. It indicates that coal permeability decreases for high confining pressures (> 5 MPa) when the gas pressure is lower. When the pore pressure is larger than 2 MPa, the permeability data are distributed both in the upper and the

Table 1
Experimental measurement details during gas injection for CCP tests.

Authors	Year	Coal rank	Origin	Sample size	Gas	Method	Pore pressure	Confining pressure	Permeability	Temp.	Equilibrium Time	Note
Harpalani and Zhao	1989	n/a	Black Warrior basin, America	Plugs: D: 38.1 mm, L:76.2 mm	CH_4; He	Steady state	0.8–6.2 MPa	11.72 MPa	0.47–11.04µD	n/a	n/a	✓
Harpalani and Schraufnagel	1990b	n/a	Piceance basin, Colorado, America; Black Warrior basin, America	Plugs: D: 38.1 mm, L:76.2 mm	CH_4; He	Steady state	1.65–6.16 MPa; 1.42–6.70 MPa	10.3; 11.7 MPa	0.53–2.04 µD; 0.32–1.78µD	n/a	n/a	✓
Robertson and Christiansen	2005	High-volatile bituminous coal; Subbituminous, low-contaminant coal	Gilson seam, Book Cliffs coal field, Uinta-Piceance basin, Utah, America; Anderson seam, Powder River basin, Gillette, Wyoming, America	Plugs: D: 50.8 mm	N_2; CH_4; CO_2	Steady state	0.48–5.58 MPa	6.895 MPa	57–292 mD; 0.0177–0.08534 mD	26.7 °C	24 h when changing gas type	✓
Guo et al.	2007	Sub-bituminous coal	Mannville Group, Alberta, Canada	Plugs: D: 33.75 mm, L:85.5 mm	CO_2	Steady state	2.2–5.6 MPa	10.5 MPa	0.03–0.05 mD	23 °C	n/a	✓
Pini et al.	2009	High volatile C bituminous coal	Monte Sinni coal mine in the Sulcis Coal Province, Sardinia, Italy	Plugs: D: 25.4 mm, L:36 mm	N_2; He; CO_2	Pressure transient	0.48–7.75 MPa	6–14 MPa	0.05–12.07D	45 °C	≥ 2 days	✓
Han et al.	2010	Anthracite coal	Yangquan coal, Qinshui Basin, China	Plugs: D: 28.5 mm, L:21.2 mm	Ar	Steady state	0.2–4.2MPa	10–40 MPa	2.1–1102.0 nD	45 °C	n/a	Samples with and without cleats
Wang et al.	2011	Anthracite coal	Northumberland Basin, Mount Carmel, Pennsylvania, America	Plugs: D: 25 mm, L:25–50 mm	He; CH_4; CO_2	Pressure transient	1.0–5.6 MPa	6–12 MPa	0.67nD– 1.65 mD	n/a	n/a	Fractured coals with different fracture geometry and water-content
Kumar et al.	2012	Subbituminous/ bituminous coal	Uinta basin, Colorado, America	Plugs: D: 25 mm, L: 50 mm	He; CH_4; CO_2	Pressure transient	1.6–5.7 MPa	10 MPa	0.01–6.63 mD	n/a	4 h for CH_4, and CO_2	Samples with different moisture levels
Vishal et al.	2013	Bituminous coal	Jharia coalfield, India	Plugs: D: 39 mm	CO_2	Steady state	1.0–5.0 MPa	5–13 MPa	0.04–31.0 mD	26 °C	n/a	✓
Gensterblum et al.	2014	Sub-bituminous coal	Walloon Subgroup in Surat Basin, Queensland, Australia	Plugs: D:38 mm, L:18.68–24.9 mm	He; Ar	Steady state	0.11–0.57 MPa	7.5–19.2 MPa	0.59–4.95 mD	35 °C	n/a	✓
Niu et al.	2014	Lignite coal	Yuanbaoshan area, Mongolia, China	Plugs: D:50 mm, L:100 mm	N_2	Steady state	0.5–1.5 MPa	8.5 MPa	13.8–33.3 mD	25, 50 °C	15 min	✓
Ranathunga et al.	2014	n/a	Hazelwood open cut mine, Gippsland, Australia	Plugs: D:25 mm, L:50 mm	CO_2; N_2	Steady state	5.0–8.0 MPa	10 MPa	0.18–0.35µD	25, 40 °C	n/a	✓
Kumar et al.	2015	Bituminous coal; Anthracite coal	Bituminous coal from the Uinta Basin, Colorado; Anthracite from Pennsylvania, America	Plugs: D: 25 mm; L:50 mm	He; CO_2	Pressure transient	1.0–6.8 MPa; 1.0–5.5 MPa	10 MPa	1.4–38.0 mD; 0.34–3.3 mD	20 °C	n/a	Propped artificial fractures in coal
Meng et al.	2015	n/a	Xuandong coal mine, China	Plugs: D: 50 mm, L:100 mm	He; CH_4; CO_2	Steady state	0.3–2.0 MPa	3.5 MPa	0.047–0.837µD	11.5 °C	n/a	✓
Qiu et al.	2017	Bituminous coal	Southeast Ordos Basin, China	Plugs: D: 25 mm, L:25–50 mm	He; CO_2	Steady state; Pressure transient	1.3–4.3 MPa	4, 6 MPa	3.9–13.5µD	n/a	n/a	✓
Wang et al.	2017b	Anthracite coal	Chang Cun coal mine, Chang Zhi City, Shan Xi Province, China	Plugs: D: 50 mm, L:100 mm	He; CH_4; CO_2	Steady state	0.5–3.0 MPa	4, 8 MPa	0.0815–0.3426 mD	20, 40 °C	0.06–12.5 h	✓
Bottomley et al.	2017	n/a	Walloon Coals, Surat Basin	Cube: l=h=w: 40 mm	He	Steady state	0.2–1.5 MPa	4 MPa	1.5–2.6 mD	n/a	n/a	✓

"n/a" represents the data is not available.

lower part of the $k/k_0 = 1$ line. When the confining pressure is between 5 and 10 MPa, the permeability data are distributed in a wide range. When the confining pressure is larger than 10 MPa, most permeability date are distributed in the lower zone.

According to the magnitude of confining pressure, the distribution of permeability ratios can also be divided into different zones for the case of gas depletion. When the confining pressure is larger than 12 MPa, the permeability ratio first slightly decreases with the decreasing of pore pressure and then increases sharply with the decreasing of pore pressure. When the confining pressure ranges from 9 to 12 MPa, the data distribute in the middle part of the graph. The permeability ratio firstly decreases with the decreasing of pore pressure and then increases slowly with the decreasing of pore pressure. When the confining pressure is lower than 9 MPa, the data spread nearly the entire graph. The permeability ratio firstly decreases with the decreasing of pore pressure, then keep slowly decreases or increases slowly with the decreasing of pore pressure.

2.3. Impact of gas characteristics

According to the characteristics of gas, permeability data distribution can be divided to two distinct zones. When the injected gas is non-adsorbing (Ar & He), most permeability ratio data are distributed in the upper part of the graph. When the injected gas is adsorbing (N_2, CH_4, CO_2), most permeability ratio data are distributed in the lower part of the graph.

For the case of gas depletion, permeability data distribution can also be divided into three zones according to gas characteristics. For permeability data of CH_4, they are distributed in the upper part of the graph. The permeability ratio firstly decreases with the decreasing of pore pressure, then increases slowly with the decreasing of pore pressure. For permeability data of He, permeability data distribute in the lower part of the graph. The permeability ratio decreases with the decreasing of pore pressure and nearly shows no rebound. For permeability data of CO_2, only one group of experiment data was tested with CO_2. The permeability ratio first decreases quickly with the decreasing of pore pressure and then shows an obvious rebound.

3. Experimental permeability under constant effective stress

3.1. Data collection

In this section, we collected the experimental permeability data under the condition of constant effective stress. In these experiments, the difference between the confining pressure (green line) and the pore pressure (black line) was maintained as constant (red line), as shown in Fig. 5. This was achieved through a same increment/decrement was applied to both the confining pressure and the pore pressure. The gray rectangular in the pore pressure line is the equilibrium stage, and the blue rectangular in the pore pressure line is the measured stage for each data point (red point) at time t_{data-x}. Permeability was measured either by the steady-state method or the pressure transient one.

For one particular experiment, a series of pressure increments/decrements was conducted. The gas pressure increases/decreases from the lowest/highest magnitude to a highest/lowest one. In our review of these experimental data, we use the permeability ratio of the permeability at the lowest gas pressure to that at a new pressure. The relations between experimental permeability data and gas pressures under the constant effective stress are shown in Fig. 6 where the details of the data sources are shown in Table 3. When the CO_2 is in supercritical phase the permeability will decrease more with injection pressure.[59–61]

As shown in Fig. 6, nearly all experimental permeability ratios under constant effective stress are greater than zero but less than unity. These experimental data represent a wide range of permeability measurements with different gases helium, argon, nitrogen, and carbon
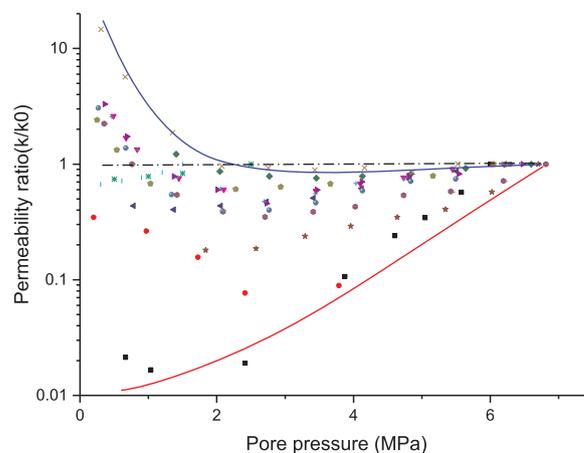
Fig. 4. Statistical distribution of coal permeability ratios during gas depletion for CCP tests.

dioxide. The injection pressure varies from 0.1 to 13.4 MPa while the effective stress from 1.0 to 16.0 MPa.

3.2. Impact of effective stress

Permeability ratios spread over all spaces between the no change line ($k/k_0 = 1$) and zero line under the condition of constant effective stress for different magnitude of effective stress. This indicates that permeability decreases irrespective of the effective stress magnitudes.

3.3. Impact of gas characteristics

As shown in Fig. 7, most permeability ratios decrease faster for the strongly adsorbing gas such as CO_2 and CH_4 (red broken circle) than the weakly adsorbing gas N_2 and non-adsorbing gas Ar & He (green broken circle). This indicates that the permeability change under constant effective stress is strongly related to the absorptivity of the injected gas. The stronger the adsorption capacity of the injected gas, the faster the permeability decreases.

4. Mechanistic analysis

According to the poroelastic solutions the permeability is a function of effective strain only. In this section a conceptual model of fracture permeability under the influence of matrix deformation is introduced, and applied to analyze the mechanisms of permeability ratio distributions under different conditions.

4.1. Solutions of single poroelasticity

Coal is a typical dual porosity/permeability system containing porous matrix surrounded by fractures. In this study the cleat system, fractures, joints, and faults are uniformly called the fracture system. It is commonly assumed that Darcy flow is a result of flow in the fracture system and that the contribution of flow in the coal matrix to Darcy flow can be neglected.[62] Thus the permeability of a coalbed is a function of its fracture system.[63–66] The permeability of fracture system is much larger than the matrix system. In order to analyze the permeability, we treat the fracture system as pore system and the matrix system as the solid parts. According to our previous work,[67,68] coal permeability can be defined as

$$\frac{k}{k_0} = \left(1 + \frac{\alpha}{\phi_{f0}}\Delta\varepsilon_e\right)^3$$

$$\text{(4)}$$

Table 2
Experimental measurement details during gas depletion for CCP tests.

Authors	Year	Coal rank	Origin	Sample size	Gas	Method	Pore pressure	Confining pressure	Permeability	Temp.	Equilibrium Time	Note
Harpalani and Zhao	1989	n/a	Black Warrior basin, America	Plugs: D: 38.1 mm, L:76.2 mm	CH₄; He	Steady state	0.36–6.6 MPa	11.7 MPa	0.21–14.69 μD	n/a	n/a	/
Harpalani and Schraufnagel	1989	n/a	Piceance basin, Colorado, America	Plugs: D: 38.1 mm, L:76.2 mm	CH₄	Steady state	0.25–6.29 MPa	7.8–13.8 MPa	0.2–10.0 μD	n/a	24 h when changing hydrostatic stress	/
Harpalani and Schraufnagel	1990a	n/a	Piceance basin, Colorado, America	Plugs: D: 38.1 mm, L:76.2 mm	CH₄	Steady state	0.38–6.83 MPa	10.3 MPa	1.0–6.3 μD	n/a	8–10 h	/
Harpalani and Schraufnagel	1990b	n/a	Piceance basin, Colorado, America; Black Warrior basin, America	Plugs: D: 38.1 mm, L:76.2 mm	CH₄; He	Steady state	0.35–6.81 MPa; 1.84–6.70 MPa	10.3; 11.7 MPa	2.82–6.29 μD; 0.32–1.78 μD	n/a	8–10 h	/
Wang et al.	2015	Anthracite coal	Jeddo coal mine, Hazleton, Luzerne County, Pennsylvania, America	Plugs: D: 25.4 mm, L:50.8 mm	He; CO₂	Pressure transient	0.2–6.0 MPa	6.9 MPa	0.02–10.46 μD	23 °C	n/a	/
Danesh et al.	2017	A high-volatile bituminous coal	Bowen Basin, Australia	Plugs: D: 61 mm, L:95 mm	CH₄	Steady state	0.5–2.5 MPa	3 MPa	4.14–5.60 mD	35 °C	9–17 days	Permeability was measured at stages where strain rate approximately zeroed due to equilibrium of desorption process and effective stress
Bottomley et al.	2017	n/a	Walloon Coals, Surat Basin	Cube: l = h = w: 40 mm	CH₄	Steady state	0.3–1.5 MPa	4 MPa	1.5–2.3 mD	n/a	n/a	/

"n/a" represents the data is not available.
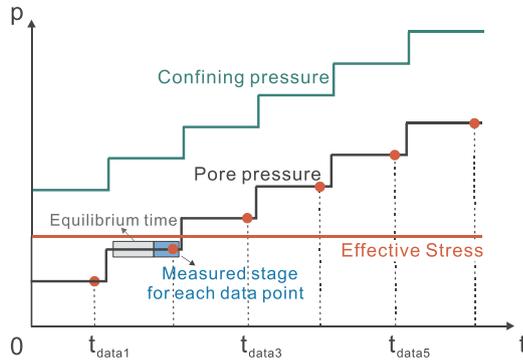
Fig. 5. Schematic diagram of the experimental process for CES tests.

$$\Delta\varepsilon_e = \Delta\varepsilon_v - \Delta\varepsilon_s - \Delta\varepsilon_d \tag{5}$$

or

$$\Delta\varepsilon_e = -\frac{\Delta\overline{\sigma} - \Delta p}{K} \tag{6}$$

where k is the permeability of coal sample, k_0 is the initial permeability of coal sample, α is the Biot coefficient, ϕ_{f0} is the initial fracture system porosity, $\Delta\varepsilon_e$ is the total effective volumetric strain, $\Delta\varepsilon_v$ is total volumetric strain increment, K is the bulk modulus of coal, $\overline{\sigma}$ is the mean confining pressure, p is the injected pore pressure, $\Delta\varepsilon_s$ is the gas sorption-induced volumetric strain, $\Delta\varepsilon_d$ is the gas diffusion-induced volumetric strain, that caused by gas diffusion from fracture to matrix induced matrix swelling.

Substituting Eq. (6) into Eq. (4), we obtain

$$\frac{k}{k_0} = \left(1 + \frac{\alpha}{\phi_{f0}}\left(-\frac{\Delta\overline{\sigma} - \Delta p}{K}\right)\right)^3 \tag{7}$$

This model is derived based on the fundamental principles of poroelasticity with the following assumptions [67]: coal is a homogeneous, isotropic and elastic continuum; strains are much smaller than the length scale; gas contained within the pores is ideal, and its viscosity is constant under isothermal conditions; the rate of gas flow through the coal is defined by Darcy's law; conditions are isothermal, coal is saturated by gas.

When the mean confining pressure remains unchanged, $\Delta\overline{\sigma} = 0$, we obtain

$$\frac{k}{k_0} = \left(1 + \frac{\alpha}{\phi_{f0}}\left(\frac{\Delta p}{K}\right)\right)^3 \tag{8}$$
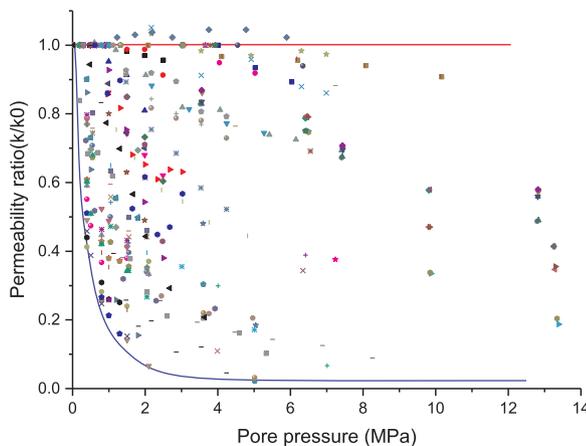
Fig. 6. Statistical graph of the coal permeability ratio on the impact of pore pressure for CES tests.

When the effective stress remains unchanged, $\Delta\overline{\sigma} - \Delta p = 0$, we obtain

$$\frac{k}{k_0} = \left(1 + \frac{\alpha}{\phi_{f0}}\left(\frac{0}{K}\right)\right)^3 = 1 \tag{9}$$

According to Eqs. (8) and (9), if we assume case A $\phi_{f0} = 0.001 \quad K = 2700\, MPa$ (high coal rank) or case B $\phi_{f0} = 0.01 \quad K = 270\, MPa$ (low coal rank) then we can get the theoretical solution of the two different types of the stress-controlled experiments, constant confining pressure (CCP) tests and constant effective stress (CES) tests, as shown in Fig. 8.

4.2. Comparison with experimental data

According to the solutions of single poroelasticity as illustrated in Fig. 8, coal permeability increases monotonically during the injection for constant confining pressure tests, remains unchanged with the gas pressure for constant effective stress tests, and decreases monotonically during the depletion. These solutions are derived on the equilibrium condition when pressures in both matrix and fracture are equalized. All permeability measurements were also conducted under the same equilibrium assumption. Our hypothesis is that experimental data should match with the analytical solutions if this equilibrium assumption was valid for both the analytical solutions and the experimental measurements. In the following, we check this hypothesis by comparing these solutions with experimental data as presented above.

4.2.1. CCP tests for gas injection
As shown in Fig. 3, coal permeability ratios change within a wide range from significant reduction (the ratio is less than 1) to enhancement (the ratio is larger than 1). When the equilibrium condition is met, the whole coal sample swells and so does each component. This represents the maximum enhancement of permeability for each gas pressure. Therefore, the analytical solution is the upper envelop of the permeability distribution. The fact that all permeability data is below this line suggests that permeability measurements were conducted under the non-equilibrium condition.

4.2.2. CCP tests for gas depletion
As shown in Fig. 4, coal permeability ratios change also within a wide range from significant reduction (the ratio is less than 1) to enhancement (the ratio is larger than 1). When the equilibrium condition is met, the whole coal sample shrinks and so does each component. This represents the maximum reduction of permeability for each gas pressure. Therefore, the analytical solution is the lower envelop of the permeability distribution. The fact that all permeability data is above this line suggests that permeability measurements were conducted also under the non-equilibrium condition.

4.2.3. CES tests
As shown in Figs. 6–7, coal permeability ratios change within a wide range from significant reduction (the ratio is less than 1) to no-change (the ratio is equal to 1). When the equilibrium condition is met, the whole coal sample remains unchanged. This represents the maximum change of permeability for each gas pressure. Therefore, the analytical solution is the upper envelop of the permeability distribution. The fact that nearly all permeability data is below this line suggests that permeability measurements were conducted under the non-equilibrium condition.

4.3. A conceptual model of mechanistic analysis

The analysis above has proved that permeability measurements were conducted under the non-equilibrium condition. This suggests that the interactions between matrixes and fractures must be taken into

Table 3
Experimental measurement details for CES tests.

Authors	Year	Coal rank	Origin	Sample size	Gas	Method	Pore pressure	Effective stress	Permeability	Temp.	Equilibrium Time	Note
Harpalani and Chen	1997	n/a	San Juan Basin, America	Plugs: D:89 mm	He	Pressure transient	0.6–6.2 MPa	5.4 MPa	0.02–0.4 mD	44.4 °C	≥ 3 days	/
Al-hawaree	1999	Bituminous coal	Coal Valley and Cardinal River mines, Hinton, Canada	Plugs: D:25.4 mm, L:38.1–63.5 mm	CO_2	Steady state	3.7–7.2 MPa	6.0, 10.0, 16.0 MPa	1.1–143.2 mD	52 °C	n/a	/
Lin et al.	2008	n/a	Wyodak-Anderson coal zone, Powder River basin, America	Plugs: D:28 mm, L:70 mm	N_2; CH_4; CO_2	Steady state	0.5–7.0 MPa	2.76 MPa	0.19–19.78 mD	22 °C	> 2 h	Coal pack
Pan et al.	2010	Bituminous coal	Bulli seam, southern Sydney basin, Australian	Plugs: D:45 mm, L:105 mm	He; CH_4; CO_2	Pressure transient	0.9–13.4 MPa	2.0–6.0 MPa	0.05–0.97 mD	45 °C	n/a	/
Chen et al.	2011	Bituminous coal	The Bulli seam in southern Sydney basin, Australian	Plugs: D:45–45.5 mm, L:101–105.5 mm	He; CH_4; CO_2	Pressure transient	0.9–13.3 MPa	2.0–6.0 MPa	0.01–0.97 mD	35, 45 °C	A few days to a few weeks	/
Li et al.	2013	Anthracite coal	Tang' an, Yong' an and Gushuyuan coal mines, southern Qinshui basin, China	Plugs: D:25.3 mm; L: 25.41–42.18 mm	CO_2	Steady state	0.2–2.1 MPa	2.2–4.0 MPa	0.07–13.59 μD	26 °C	n/a	/
Xu et al.	2013	Anthracite coal	Zhaozhuang coal mine in Jincheng, Southern Qinshui basin, China	Plugs: D:50 mm, L:100 mm	CH_4; CO_2	Steady state	0.3–2.0 MPa	1.0–5.0 MPa	0.06–0.99 mD	n/a	n/a	/
Lin and Kovscek	2014	n/a	Wyodak Anderson coal zone, Powder River Basin, Montana	Plugs: D:25.4 mm, L:25–75 mm	N_2; He; CO_2	Steady state; Pressure transient	0.1–6.2 MPa	3.0 MPa	0.6–18.0 mD	22 °C	n/a	Gas pressure decrease – 2 group of data, 7 in total
Seomoon et al.	2015	Bituminous coal	East Kalimantan, Indonesia	Plugs: D:38.1 mm, L:108.3 mm	CH_4; CO_2	Steady state	0.6–3.0 MPa	2.07 MPa	1.6–5.3 mD	15 °C	n/a	/
Li et al.	2015	Anthracite coal	Yong'an mine, southeastern Qinshui basin, China	Plugs: D:25.4 mm, L:35.4 mm	CO_2	Steady state	0.2–2.1 MPa	2.2–4.0 MPa	4.34–20.13 μD	26 °C	n/a	Gas pressure decrease
Anggara et al.	2016	Low rank ranging from lignite to sub-bituminous coal	Kushiro coal mine, Hokkaido, Japan	Plugs: D:50 mm, L:100 mm	He; CH_4; CO_2	Steady state	0.5–2.5 MPa	2.0–4.0 MPa	0.015–0.229 mD	n/a	48 h	/
Meng and Li	2017	Anthracite coal	Permian Shanxi Formation, southern Qinshui Basin	Plugs: D:25 mm, L:46 mm	N_2; CH_4; CO_2	Pressure transient	1.0–7.0 MPa	3.5 MPa	1.0–23.1 mD	20 °C	12–24 h	/
Feng et al.	2017	n/a	San Juan coal	D:51 mm, L:89 mm	CH_4	Pressure transient	0.34–8.5 MPa	5.5 MPa	n/a	n/a	5 days	Gas pressure decrease

"n/a" represents the data is not available.
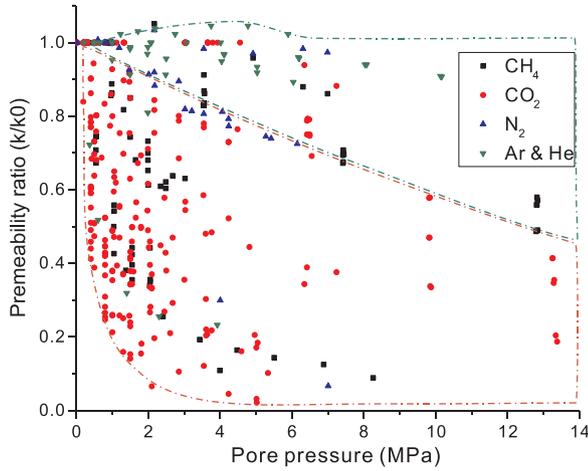
Fig. 7. Gas composition analysis of CES tests.

consideration to fully understand the distribution of permeability ratios. We use the injection of an adsorbing gas (such as CO_2) as an example to illustrate how the mass transfer and the stress transfer between the matrix and the fracture are coupled under the constant confining pressure conditions, as shown in Fig. 9. The sample is placed into the triaxial core holder and both confining pressure (σ_c) and axial stresses (σ_h) are applied to establish initial condition and kept constant ($\Delta\bar{\sigma} = 0$). The injected pore pressure is kept constant ($\Delta p = 0$). We take the A-A` cross-section to analyze the deformation of the sample. We use the ellipse to represent the fracture and the bubble to represent the smallest component of the matrix system around the fracture. According to our previous work,[68,69] evolution of coal permeability can be divided as three distinct stages. Prior to injection, the coal is under an equilibrium state (pressure, stress and mass contents) and no interactions between the matrix and the fracture occur. Post-injection, a series of processes initiate. First, gas instantly invades the fracture due to its relatively high permeability. We use this condition as a starting point ($t = t_s$), to explain how does the permeability changes over time. As result of this process, a pressure difference between the matrix and the fracture is created – resulting in the diffusion of gas from the fracture into the matrix, as shown in Fig. 9(a). As the gas molecules attach to the fracture surface and diffuse into the matrix, local strain evolves in the matrix due to both the gas adsorption and the increased gas pressure. Under this condition, the matrix swells (dark gray bubble) while the fracture narrows as shown in Fig. 9(b). Because this also occurs locally in the vicinity of the fracture, the decrease in volume of the fracture must be equal to the swelling volume of the matrix. As a result of the widening of the swelling zone, the fracture permeability recovers at
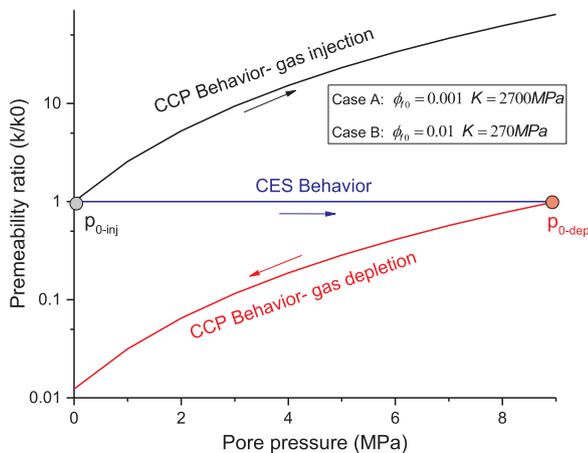
Fig. 8. Example analytical solutions of CCP and CES tests.

time t_m, which is the turning time of the permeability ratio. As the gas diffuses further into the whole matrix of the sample, the gas pressure propagates throughout the matrix until a new equilibrium state between the fracture and the matrix is reached at time t_f, as shown in Fig. 9(c). In this condition, the entire matrix swells, so does the fracture as shown in Fig. 9(c).

As illustrated in Fig. 9, coal permeability is a function of time for a constant gas injection pressure. The magnitude of permeability for the injection pressure varies over a wide range of magnitudes from reduction (the ratio is less than 1) to enhancement (the ratio is larger than 1). Each point corresponds a state (initial state, transient state, or final equilibrium state). In this study, we define the permeability at the final equilibrium state as equilibrium permeability and that at the transient state as non-equilibrium permeability. With these definitions, we can establish the relation between the analytical solutions and experimental measurements. All these solutions are for the equilibrium permeability while experimental measurements are a mixture of equilibrium permeability and non-equilibrium permeability.

When the matrix permeability is very high (micro-crack developed or matrix permeability high), gas can diffuse from fractures into matrixes. Under this condition, the time from the initial equilibrium to the final one is short, and can be neglected. This represents the upper bound of the permeability change. When the matrix permeability is extremely low, the time from the initial equilibrium to the final one is long and cannot be neglected. If this time is extremely long, gas diffusion-induced swelling may take place only in the vicinity of fracture walls. Under this condition, coal permeability is controlled primarily by the local deformation. 100% of coal swelling/shrinkage would contribute to the reduction of coal permeability provided that the fractures are much more compliant than the coal matrix.[54,70,71] The analytical solution of this situation represents the lower bound of the permeability change. In this case, the total volumetric strain is defined as

$$\Delta\varepsilon_v = 0 \tag{10}$$

From Eq. (5)

$$\Delta\varepsilon_e = -\Delta\varepsilon_s - \Delta\varepsilon_d \tag{11}$$

Substituting Eq. (11) into Eq. (4) gives

$$\frac{k}{k_0} = \left[1 - \frac{\alpha}{\phi_{f0}}(\Delta\varepsilon_s + \Delta\varepsilon_d)\right]^3 \tag{12}$$

The permeability ratio is controlled by the gas sorption-induced volumetric strain ($\Delta\varepsilon_s$) and the gas diffusion-induced volumetric strain ($\Delta\varepsilon_d$). The relations are

$$\varepsilon_s = \varepsilon_L \frac{p}{P_L + p} \tag{13}$$

$$\varepsilon_d = f(p - p_0) \tag{14}$$

where the Langmuir volumetric strain, ε_L, is a constant representing the volumetric strain at infinite pore pressure and the Langmuir pressure constant, P_L, representing the pore pressure at which the measured volumetric strain is equal to $0.5\varepsilon_L$. The free swelling model (Eq. (7)) and constant volume model (Eq. (12)) are the upper bound and the lower bound of the permeability change. For a particular experimental measurement, coal permeability would be in-between, as shown by gray areas in Figs. 10–12 for the cases of gas injection in CCP tests, gas depletion in CCP tests, and all CES tests. In this study, the area of permeability change bounded by the analytical solution of free swelling and by that of constant volume is defined as a permeability map.

Comparing Fig. 7 with Fig. 12, we can find that the distribution of permeability ratios for the cases of absorbing gas is more closely to the constant volume behavior, while the distribution of permeability ratios for the cases of non-absorbing gas is more closely to the free swelling behavior.

Permeability is a function of effective stress (effective strain). In CES
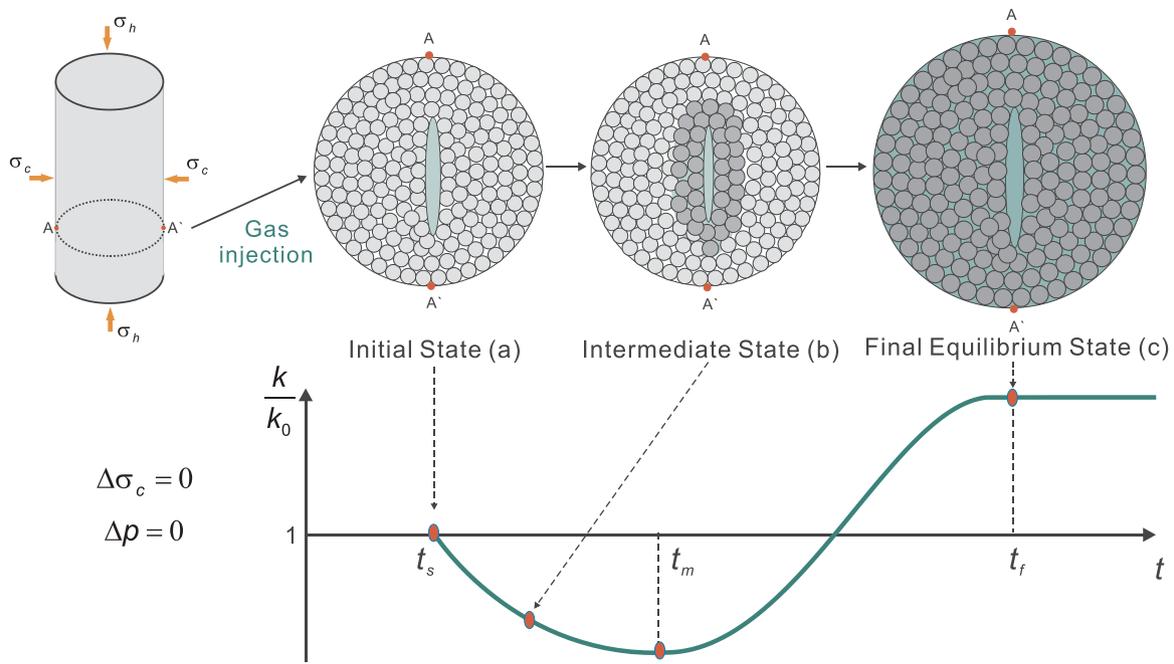
Fig. 9. Illustration of relations between gas diffusion in the matrix and fracture opening under the stress-controlled conditions.
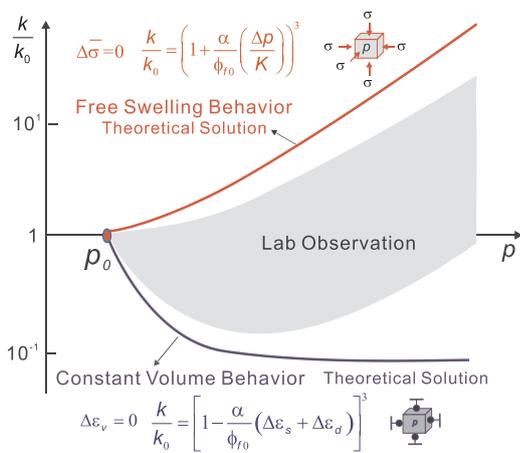
Fig. 10. Map of permeability change during gas injection for CCP tests.
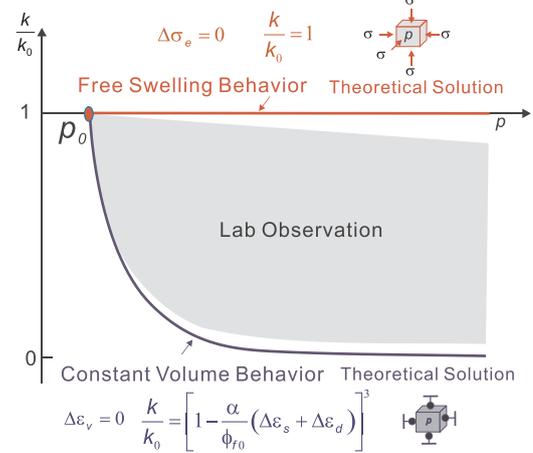
Fig. 12. Map of permeability change for CES tests.
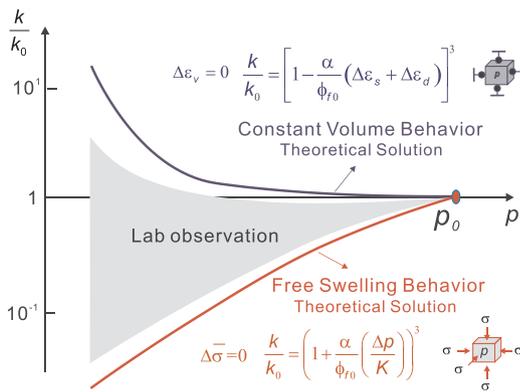
Fig. 11. Map of permeability change during gas depletion for CCP tests.

tests, the effective stress in the fracture was maintained as constant while the effective stress in the matrix evolves as the interaction between matrix and fracture progresses. This interaction determines the permeability map. In CCP tests, we can find that the distribution of

permeability ratios for high confining pressures is more closely to the constant volume behavior, while the distribution of that for low confining pressures is more closely to the free swelling behavior.

5. Conclusions

Through comparing the experimental data of coal permeability evolutions under both constant confining pressures and constant effective stresses, the following conclusions can be drawn:

- Experimental permeability data were obtained under the common assumption of the equilibrium between coal matrix and fracture pressures, but not consistent with the analytical solutions under the same assumption. For a constant fracture pressure, coal permeability still changes due to the gas diffusion from fractures into matrixes. The permeability stabilizes when the fracture pressure is equalized with the matrix pressure. This process may take a very long time because of low matrix permeability, and the equilibrium condition may never be met in all of these laboratory tests.
- Permeability data for both constant confining tests and constant effective stress tests are confined within the poroelastic solutions for

two extreme boundary conditions: free-swelling and zero-swelling. Evolutions of coal permeability between these poroelastic solutions are primarily determined by the matrix-fracture interactions, including sorption-induced swelling/shrinking, through transient effective stresses in matrixes and fractures.

Acknowledgements

References

1. Seidle JR, Huitt L. Experimental measurement of coal matrix shrinkage due to gas desorption and implications for cleat permeability increases. In: International meeting on petroleum Engineering. Beijing; 14–17 November 1995:575–82.
2. Pan Z, Connell LD, Camilleri M. Laboratory characterisation of coal reservoir permeability for primary and enhanced coalbed methane recovery. *Int J Coal Geol.* 2010;82(3):252–261.
3. Palmer I, Mansoori J. How permeability depends on stress and pore pressure in coalbeds: a new model. In: SPE Annual Technical Conference and Exhibition; 1996.
4. Gilman A, Beckie R. Flow of coal-bed methane to a gallery. *Transp Porous Media.* 2000;41(1):1–16.
5. Cui X, Bustin RM. Volumetric strain associated with methane desorption and its impact on coalbed gas production from deep coal seams. *AAPG Bull.* 2005;89(9):1181–1202.
6. Shi JQ, Durucan S. Modelling laboratory horizontal stress and coal permeability data using S&D permeability model. *Int J Coal Geol.* 2014;131:172–176.
7. Zimmerman RW. Pore volume and porosity changes under uniaxial strain conditions. *Transp Porous Media.* 2017;119(2):481–498.
8. Robertson EP, Christiansen RL. *A permeability model for coal and other fractured, sorptive-elastic media.* Idaho National Laboratory (INL); 2006.
9. Mitra A, Harpalani S, Liu S. Laboratory measurement and modeling of coal permeability with continued methane production: part 1-Laboratory results. *Fuel.* 2012;94(1):110–116.
10. Wang Y, Liu S, Elsworth D. Laboratory investigations of gas flow behaviors in tight anthracite and evaluation of different pulse-decay methods on permeability estimation. *Int J Coal Geol.* 2015;149:118–128.
11. Fan L, Liu S. Numerical prediction of in situ horizontal stress evolution in coalbed methane reservoirs by considering both poroelastic and sorption induced strain effects. *Int J Rock Mech Min Sci.* 2018;104:156–164.
12. Harpalani S, Zhao X. The unusual response of coal permeability to varying gas pressure and effective stress. In: Proceedings of the 30th US Symposium on Rock Mechanics (USRMS). Morgantown; 19–22 June 1989:65–72.
13. Harpalani S, Schraufnagel RA. Shrinkage of coal matrix with release of gas and its impact on permeability of coal. *Fuel.* 1990;69(5):551–556.
14. Robertson EP, Christiansen RL. *Modeling permeability in coal using sorption-induced strain data.* Idaho National Laboratory (INL); 2005.
15. Pini R, Ottiger S, Burlini L, Storti G, Mazzotti M. Role of adsorption and swelling on the dynamics of gas injection in coal. *J Geophys Res.* 2009;114(B4).
16. Gensterblum Y, Ghanizadeh A, Krooss BM. Gas permeability measurements on Australian subbituminous coals: fluid dynamic and poroelastic aspects. *J Nat Gas Sci Eng.* 2014;19:202–214.
17. Meng J, Nie B, Zhao B, Ma Y. Study on law of raw coal seepage during loading process at different gas pressures. *Min Sci Technol (China).* 2015;25(1):31–35.
18. Harpalani S, Schraufnagel RA. Flow of methane in deep coal seams. In: ISRM International Symposium. Pau; 30 August-2 September 1989.:195–201.
19. Qiu Y, Li Z, Hao S. Comparison between steady state method and pulse transient method for coal permeability measurement. in: IOP Conference Series: Earth and Environmental Science. 64. Ordos; 14–16 April 2017:1–6.
20. Bottomley W, Furniss J, Raza SS, Ge L, Rudolph V. Characterising the Dependence of Coal Permeability to Methane Adsorption, Pore Pressure and Stress: Laboratory Testing of Walloon Coals from the Surat Basin. in: SPE/IATMI Asia Pacific Oil & Gas Conference and Exhibition. Jakarta; 17–19 October. 2017:1–16.
21. Wang K, Du F, Wang G. Investigation of gas pressure and temperature effects on the permeability and steady-state time of chinese anthracite coal: an experimental study. *J Nat Gas Sci Eng.* 2017;40:179–188.
22. Kumar H, Elsworth D, Liu J, Pone D, Mathews JP. Optimizing enhanced coalbed methane recovery for unhindered production and CO₂ injectivity. *Int J Greenh Gas Control.* 2012;11:86–97.
23. Guo R, Mannhardt K, Kantzas A. Laboratory investigation on the permeability of coal during primary and enhanced coalbed methane production. in: Canadian International Petroleum Conference. Calgary; 12–14 June:p. 2007. :1-8.
24. Vishal V, Ranjith P, Pradhan S, Singh T. Permeability of sub-critical carbon dioxide in naturally fractured Indian bituminous coal at a range of down-hole stress conditions. *Eng Geol.* 2013;167:148–156.
25. Ranathunga AS, Perera SA, Gamage RP. An Experimental Study to Investigate the Temperature Effect on Permeability of Victorian Brown Coal during CO 2 Sequestration. In: ISRM International Symposium-Proceedings of the 8th Asian Rock Mechanics Symposium. Sapporo; 14-16 October 2014.:2851–7.
26. Niu S, Zhao Y, Hu Y. Experimental ivestigation of the temperature and pore pressure effect on permeability of lignite under the in situ condition. *Transp Porous Media.* 2014;101(1):137–148.
27. Wang S, Elsworth D, Liu J. Permeability evolution in fractured coal: the roles of fracture geometry and water-content. *Int J Coal Geol.* 2011;87(1):13–25.
28. Han F, Busch A, Krooss BM, Liu Z, van Wageningen N, Yang J. Experimental study on fluid transport processes in the cleat and matrix systems of coal. *Energy Fuels.* 2010;24(12):6653–6661.
29. Klinkenberg L. The permeability of porous media to liquids and gases. in: Drilling and production practice. New York, USA; 1 January 1941 :200–13.
30. Kumar H, Elsworth D, Liu J, Pone D, Mathews JP. Permeability evolution of propped artificial fractures in coal on injection of CO 2. *J Pet Sci Eng.* 2015;133:695–704.
31. Mazumder S, Wolf KH. Differential swelling and permeability change of coal in response to CO 2 injection for ECBM. *Int J Coal Geol.* 2008;74(2):123–138.
32. Siriwardane H, Haljasmaa I, McLendon R, Irdi G, Soong Y, Bromhal G. Influence of carbon dioxide on coal permeability determined by pressure transient methods. *Int J Coal Geol.* 2009;77(1):109–118.
33. Liu Q, Cheng Y, Ren T, Jing H, Tu Q, Dong J. Experimental observations of matrix swelling area propagation on permeability evolution using natural and reconstituted samples. *J Nat Gas Sci Eng.* 2016;34:680–688.
34. Danesh NN, Chen Z, Connell LD, Kizil MS, Pan Z, Aminossadati SM. Characterisation of creep in coal and its impact on permeability: an experimental study. *Int J Coal Geol.* 2017;173:200–211.
35. Harpalani S, Schraufnagel RA. Measurement of parameters impacting methane recovery from coal seams. *Geotech Geol Eng.* 1990;8(4):369–384.
36. Harpalani S, Chen G. Influence of gas production induced volumetric strain on permeability of coal. *Geotech Geol Eng.* 1997;15(4):303–325.
37. Lin W, Tang G-Q, Kovscek AR. Sorption-induced permeability change of coal during gas-injection processes. *SPE Reserv Eval Eng.* 2008;11(04):792–802.
38. Chen Z, Pan Z, Liu J, Connell LD, Elsworth D. Effect of the effective stress coefficient and sorption-induced strain on the evolution of coal permeability: experimental observations. *Int J Greenh Gas Control.* 2011;5(5):1284–1293.
39. Li J, Liu D, Yao Y, Cai Y, Chen Y. Evaluation and modeling of gas changes in anthracite coals. *Fuel.* 2013;111:606–612.
40. Anggara F, Sasaki K, Sugai Y. The correlation between coal swelling and permeability during CO 2 sequestration: a case study using Kushiro low rank coals. *Int J Coal Geol.* 2016;166:62–70.
41. Meng Y, Li Z. Triaxial experiments on adsorption deformation and permeability of different sorbing gases in anthracite coal. *J Nat Gas Sci Eng.* 2017;46:59–70.
42. Feng R, Harpalani S, Pandey R. Evaluation of various pulse-decay laboratory permeability measurement techniques for highly stressed coals. *Rock Mech Rock Eng.* 2017;50(2):297–308.
43. Lin W, Kovscek AR. Gas sorption and the consequent volumetric and permeability change of coal I: experimental. *Transp Porous Media.* 2014;105(2):371–389.
44. Seomoon H, Lee M, Sung W. Analysis of sorption-induced permeability reduction considering gas diffusion phenomenon in coal seam reservoir. *Transp Porous Media.* 2015;108(3):713–729.
45. Al-hawaree M. *Geomechanics of CO₂ sequestration in coalbed methane reservoirs.* University of Alberta; 1999.
46. Li J, Liu D, Lu S, Yao Y, Xue H. Evaluation and modeling of the CO₂ permeability variation by coupling effective pore size evolution in anthracite coal. *Energy Fuels.* 2015;29(2):717–723.
47. Xu J, Cao J, Li B, Zhou T, Minghui L, Dong L. Experimental research on response law of permeability of coal to pore pressure. *Chin J Rock Mech Eng.* 2013;32(2):225–230.
48. Jiang X, Jie C, Bobo L. Experimental research on response law of permeability of coal to pore pressure. *Chin J Rock Mech Eng.* 2013;32(2):225–230.
49. McKee CR, Bumb AC, Koenig RA. Stress-dependent permeability and porosity of coal and other geologic formations. *SPE Form Eval.* 1988;3(01):81–91.
50. Seidle J, Jeansonne M, Erickson D. Application of matchstick geometry to stress dependent permeability in coals. In: SPE rocky mountain regional meeting. Casper; 18-21 May 1992:433–44.
51. Shi J, Durucan S. Drawdown induced changes in permeability of coalbeds: a new interpretation of the reservoir response to primary recovery. *Transp Porous Media.* 2004;56(1):1–16.
52. Pan Z, Connell LD. A theoretical model for gas adsorption-induced coal swelling. *Int J Coal Geol.* 2007;69(4):243–252.
53. Connell LD, Lu M, Pan Z. An analytical coal permeability model for tri-axial strain and stress conditions. *Int J Coal Geol.* 2010;84(2):103–114.
54. Liu J, Chen Z, Elsworth D, Qu H, Chen D. Interactions of multiple processes during CBM extraction: a critical review. *Int J Coal Geol.* 2011;87(3):175–189.
55. Wang C, Zhai P, Chen Z, Liu J, Wang L, Xie J. Experimental study of coal matrix-cleat interaction under constant volume boundary condition. *Int J Coal Geol.* 2017;181:124–132.
56. Sander R, Pan Z, Connell LD. Laboratory measurement of low permeability unconventional gas reservoir rocks: a review of experimental methods. *J Nat Gas Sci Eng.* 2017;37:248–279.
57. Ngo VT, Lu VD, Le VM A comparison of permeability prediction methods using core analysis data for sandstone and carbonate reservoirs. Geomechanics and Geophysics for Geo-Energy and Geo-Resources:1–11.
58. Brace WF, Walsh J, Frangos W. Permeability of granite under high pressure. *J Geophys Res.* 1968;73(6):2225–2236.

59. Ranathunga A, Perera M, Ranjith P, De Silva G. A macro-scale view of the influence of effective stress on carbon dioxide flow behaviour in coal: an experimental study. *Geomech Geophys Geo-Energy Geo-Resour.* 2017;3(1):13–28.

60. Zhang X, Ranjith P, Perera M, Ranathunga A, Haque A. Gas transportation and enhanced coalbed methane recovery processes in deep coal seams: a review. *Energy Fuels.* 2016;30(11):8832–8849.

61. Jia W, McPherson B, Dai Z, Irons T, Xiao T. Evaluation of pressure management strategies and impact of simplifications for a post-EOR CO_2 storage project. *Geomech Geophys Geo-Energy Geo-Resour.* 2017;3(3):281–292.

62. Purl R, Evanoff J, Brugler M. Measurement of coal cleat porosity and relative permeability characteristics. In: SPE Gas Technology Symposium. Houston; 22–24 January 1991.

63. Palmer I. Permeability changes in coal: analytical modeling. *Int J Coal Geol.* 2009;77(1):119–126.

64. Ried G, Towler B, Harris H. Simulation and economics of coalbed methane production in the Powder River Basin. In: SPE Rocky Mountain Regional Meeting. Casper; 18–21 May 1992.:425–32.

65. Sparks D, McLendon T, Saulsberry J, Lambert S. The effects of stress on coalbed reservoir performance, Black Warrior Basin, USA. in: SPE Annual Technical Conference and Exhibition. Dallas; 22–25 October 1995:339–51.

66. Pan Z, Connell LD. Modelling permeability for coal reservoirs: a review of analytical models and testing data. *Int J Coal Geol.* 2012;92:1–44.

67. Zhang H, Liu J, Elsworth D. How sorption-induced matrix deformation affects gas flow in coal seams: a new FE model. *Int J Rock Mech Min Sci.* 2008;45(8):1226–1236.

68. Liu J, Wang J, Chen Z, Wang S, Elsworth D, Jiang Y. Impact of transition from local swelling to macro swelling on the evolution of coal permeability. *Int J Coal Geol.* 2011;88(1):31–40.

69. Liu J, Chen Z, Elsworth D, Miao X, Mao X. Evolution of coal permeability from stress-controlled to displacement-controlled swelling conditions. *Fuel.* 2011;90(10):2987–2997.

70. Harpalani S, Chen G. Estimation of changes in fracture porosity of coal with gas emission. *Fuel.* 1995;74(10):1491–1498.

71. Ma Q, Harpalani S, Liu S. A simplified permeability model for coalbed methane reservoirs based on matchstick strain and constant volume theory. *Int J Coal Geol.* 2011;85(1):43–48.